



Short communication

Exceptional methanol electro-oxidation activity by bimetallic concave and dendritic Pt–Cu nanocrystals catalysts



Ying-Xia Wang, Hui-Jing Zhou, Ping-Chuan Sun, Tie-Hong Chen*

Institute of New Catalytic Materials Science, Key Laboratory of Advanced Energy Materials Chemistry (MOE), College of Chemistry, Synergetic Innovation Center of Chemical Science and Engineering (Tianjin), Nankai University, Tianjin 300071, PR China

HIGHLIGHTS

- We report a novel one-pot co-reduction solvothermal approach to obtain concave and dendritic PtCu_x ($x = 1, 2$ and 3) bimetallic nanoparticles.
- PtCu_2/C shows exceptional catalytic activity and strong poisoning resistance in methanol oxidation.
- The specific and mass activities of PtCu_2/C were 4.1 and 3.3 times higher than those of the commercial Pt/C catalysts.

ARTICLE INFO

Article history:

Received 9 April 2013

Received in revised form

3 July 2013

Accepted 3 July 2013

Available online 12 July 2013

Keywords:

Fuel cell

Electrocatalysis

Platinum

Nanocrystals

Methanol oxidation

ABSTRACT

PtCu_x ($x = 1, 2$ and 3) bimetallic nanocrystals with concave surface and dendritic morphology were prepared and used as electrocatalysts in methanol oxidation reaction (MOR) for polymer electrolyte membrane fuel cells. The bimetallic nanocrystals were synthesized via one-pot co-reduction of H_2PtCl_6 and $\text{Cu}(\text{acac})_2$ by oleylamine and polyvinyl pyrrolidone (PVP) in an autoclave at $180\text{ }^\circ\text{C}$. The concave dendritic bimetallic nanostructure consisted of a core rich in Cu and nanodendrites rich in Pt, which was formed via galvanic replacement of Cu by Pt. It was found that PVP played an important role in initiating, facilitating, and directing the replacement reaction. The electrochemical properties of the PtCu_x were characterized by cyclic voltammetry (CV) and chronoamperometry (CA). The concave dendritic PtCu_2/C nanocrystals exhibited exceptionally high activity and strong poisoning resistance in MOR. At 0.75 V (vs. reversible hydrogen electrode, RHE) the mass activity and specific activity of PtCu_2/C were 3.3 and 4.1 times higher than those of the commercial Pt/C catalysts, respectively. The enhanced catalytic activity could be attributed to the unique concave dendritic morphology of the bimetallic nanocrystals.

© 2013 Elsevier B.V. All rights reserved.

1. Introduction

Energy is one of the biggest challenges for twenty-first century. As interest in hydrogen economy grows, research on hydrogen storage and fuel cells is expanding [1–3]. Low temperature fuel cells, such as direct methanol fuel cells (DMFCs) and direct formic acid fuel cell (DFAFCs) with unique properties such as low operating temperature and relatively high energy density, are expected to be alternative power sources for portable electronic devices [4]. DMFCs can be easily re-fueled in a short time [5], while lithium ion batteries suffer from long re-charge time. In addition, with liquid and renewable methanol as fuel, DMFCs have been considered to be a favorable option in terms of fuel usage and feed strategies [4,6,7]. The outstanding electrocatalytic activity of platinum in the methanol-oxidation reaction makes it desirable as DMFCs electrode

materials [8–12]. One of the major limitations for commercialization of this technology is that pure Pt is easily poisoned by reaction intermediates, such as CO at room or moderate temperature [13–15]. One tactic to improve the durability of electrocatalysts is to prepare Pt nanocrystals with high-index facets [16]. Another tactic is to fabricate binary platinum alloy catalysts by adding a second metal to platinum. For methanol oxidation, a number of alloys, such as PtSn , PtCo , PtNi , PtCu and so on, as low cost anode catalysts for methanol oxidation have been investigated [17–20]. More recently, it has been demonstrated that the catalytic activity of Pt-based nanocatalysts can be considerably enhanced by tuning their electronic and geometric structures with the formation of bimetallic structures [1,12].

Pt–Cu bimetallic nanocrystal is one of the most promising candidates due to its high stability against catalyst poisoning and abundant sources of copper. Preparation methods of Pt–Cu nanocrystals with various nanostructures such as nanocubes [14,21], nanospheres [22] and nanocages [23] have been developed.

* Corresponding author. Tel./fax: +86 22 23507975.

E-mail address: chenth@nankai.edu.cn (T.-H. Chen).

Concave Pt–Cu nanocrystals have shown significantly enhanced catalytic activity in methanol oxidation because of the existence of high density atomic steps, ledges and kinks on the high-index-facets [14]. Recently, dealloyed Pt–Cu alloy nanoparticles have attracted attention as electrocatalysts for proton exchange membrane fuel cell [23–29]. It has been shown that by using electrochemical or chemical methods, Cu is removed from the alloy surface layers, forming a Pt-rich core–shell nanostructure, which exhibits enhanced methanol oxidation reaction activity when compared to pure Pt nanoparticles [23].

Herein, we report the synthesis, characterization and electrochemical evaluation of concave and dendritic PtCu_x nanocrystals prepared via galvanic replacement in a one-pot organic solvothermal process. It was found that the concave and dendritic PtCu_2/C nanocrystals exhibited superior electrocatalytic activity in methanol oxidation reaction. The mass and specific activity of the PtCu_2/C reached $604.8 \text{ mA mg}^{-1} \text{ Pt}$ and 9.4 mA m^{-2} at 0.75 V (vs. reversible hydrogen electrode, RHE), which were about 3.3 times and 4.1 times higher than those of the commercial Pt/C catalyst ($185.5 \text{ mA mg}^{-1} \text{ Pt}$ and 2.3 mA m^{-2}), respectively.

2. Experimental

2.1. Chemicals and materials

Analytical grade hexachloroplatinic(IV) acid hexahydrate ($\text{H}_2\text{PtCl}_6 \cdot 6\text{H}_2\text{O}$, 99.9%), anhydrous ethanol and toluene were obtained from Tianjin Chemical Reagents, China. Oleylamine (80–90%), PVP (MW = 40,000, AR) and $\text{Cu}(\text{acac})_2$ (acac = acetylacetone) (99.9%) were purchased from Acros (Geel, Belgium). The Pt/C (20% by wt. Pt nanoparticles on Vulcan XC-72 carbon support) catalyst was purchased from Alfa Aesar (WardHill, MA, USA). Nafion (5% in a mixture of lower aliphatic alcohols and water) was purchased from Sigma Aldrich. All the chemicals were used as received without further purification. A $0.01 \text{ mol L}^{-1} \text{ H}_2\text{PtCl}_6$ solution was prepared by dissolving 0.0518 g of $\text{H}_2\text{PtCl}_6 \cdot 6\text{H}_2\text{O}$ powder in 10 mL anhydrous ethanol.

2.2. Samples preparation

2.2.1. Synthesis of concave dendritic PtCu_2

In a typical synthesis, solution A (0.03 mmol of $\text{H}_2\text{PtCl}_6 \cdot 6\text{H}_2\text{O}$ and 50 mg PVP dissolved in 5 mL anhydrous ethanol) was mixed with solution B (0.06 mmol $\text{Cu}(\text{acac})_2$ dispersed in 10 mL oleylamine). After ultrasonic treatment for about 30 min, the mixed solution was transferred into a 25 mL Teflon-lined autoclave. The autoclave was maintained at 180°C for 12 h, and then cooled down to ambient temperature. The black precipitate was washed with toluene and re-dispersed into ethanol for several times before drying at 80°C overnight.

2.2.2. Synthesis of concave dendritic PtCu and PtCu_3

Concave dendritic PtCu and PtCu_3 were prepared with a similar method for PtCu_2 but with different amounts of $\text{H}_2\text{PtCl}_6 \cdot 6\text{H}_2\text{O}$ (0.06 mmol and 0.02 mmol, respectively).

2.2.3. Synthesis of Pt_3Cu nanospheres

The synthesis of Pt_3Cu nanosphere was similar to that of PtCu_2 , but with 0.18 mmol $\text{H}_2\text{PtCl}_6 \cdot 6\text{H}_2\text{O}$ and the reaction time was extended to 24 h.

2.3. Characterization

Powder X-ray diffraction (XRD) patterns were recorded using a Bruker diffractometer with $\text{Cu K}\alpha$ radiation (D8 Advance X-ray

diffractometer, $\text{Cu K}\alpha$, $\lambda = 1.5406 \text{ \AA}$, 40 kV and 40 mA). The composition of the product was measured by the inductively coupled plasma-atomic emission spectrometer (ICP-AES; USA Thermo Jarrell-Ash Corp. ICP-9000(N+M)). Field-emission scanning electron microscopy (FESEM; JEOL, JSM-7500F, 8 kV) was used to analyze the morphology of the samples. Transmission electron microscopy (TEM), energy-dispersive X-ray spectrometry (EDS) and EELS elemental mapping observations were performed on a Philips Tecnai F20 microscope, working at 200 kV. All samples subjected to TEM measurements were dispersed in ethanol ultrasonically and were dropped on nickel grids.

2.4. Electrochemical measurements

Cyclic voltammetry (CV) and chronoamperometry (CA) measurements were performed using a three-electrode cell with a CHI660 electrochemical workstation at ambient temperature. The working electrode was a glassy carbon electrode (GCE) with a diameter of 3 mm. Before the tests, the Pt–Cu nanocrystals (NCs) were first deposited on a carbon support (Vulcan XC-72) by sonicating the mixture of NCs and carbon support (NCs/C = 4:6 by weight) in hexane/acetone (v/v = 2:1). The mixture was sonicated for 6 h and the Pt–Cu/C catalyst was separated by centrifugation, washed two times with ethanol, and dried at 70°C for overnight. The actual loadings of Pt on the carbon black measured by ICP were 9.4%, 12.6%, 15.5% and 20.1% for PtCu_3/C , PtCu_2/C , PtCu/C and $\text{Pt}_3\text{Cu}/\text{C}$, respectively. A leak-free Ag/AgCl (in saturated KCl) electrode was used as the reference and a Pt wire was used as the counter electrode. The reference electrode was calibrated with a reversible hydrogen electrode (RHE). For electrochemical measurements, 4 mg of catalyst (Pt–Cu/C or commercial Pt/C) was dispersed in 1 mL ethanol under ultrasonication for 1 h and 10 μL of the catalyst suspension was dropped onto the GCE. After drying in air for 2 h, a 5 μL Nafion (Sigma Aldrich) solution (0.2%) was added, followed by drying at ambient temperature. The dried GCE was cleaned again by sequentially washing with water. Prior to electrochemical measurements, the electrolytes were deoxygenated by bubbling with N_2 for 30 min. The methanol oxidation reaction (MOR) experiments were carried out by sweeping the potential from $+0.10 \text{ V}$ to $+1.00 \text{ V}$ at a scan rate of 20 mV s^{-1} in a solution containing 0.5 M H_2SO_4 and 1 M CH_3OH . CA curves were recorded at 0.7 V in a solution containing 0.5 M H_2SO_4 and 1 M CH_3OH for 5 h to investigate the durability of the catalysts.

For the electrochemical active surface area (ECSA) study, the CV profiles were recorded at a scan rate of 50 mV s^{-1} within the potential range from -0.05 to 1.1 V (vs. RHE) in a 0.5 M H_2SO_4 solution under a flow of N_2 . ECSA values were calculated by integrating the area under curves for the hydrogen adsorption charge (Q_H) region between -0.05 V and $+0.40 \text{ V}$ of the reverse sweep in the CV and the Q_H can be determined by using $Q_H = 0.5 \times Q$, where Q is the charge in the hydrogen adsorption/desorption area obtained after double-layer correction. The specific ECSA was calculated based on the following relation:

$$\text{specific ECSA} = Q_H/m \times q_H$$

where m is the loading amount of metal, q_H is using a conversion factor of 0.21 mC cm^{-2} for the adsorption of a monolayer of hydrogen on Pt surface, and Q_H is the charge for hydrogen adsorption, which can be calculated from the area under the CV curve by:

$$Q_H = \int IdE/\nu$$

where ν is the scanning rate.

Table 1
Composition of as-prepared Pt–Cu nanocrystals.

entry	Catalyst	Analyzed molar ratios (Pt/Cu) by EDS	Analyzed molar ratios (Pt/Cu) by ICP-AES
1	PtCu ₃	0.28:0.72	0.24:0.76
2	PtCu ₂	0.40:0.60	0.38:0.62
3	PtCu	0.55:0.45	0.52:0.48
4	Pt ₃ Cu	0.79:0.21	0.75:0.25

3. Results and discussion

The accurate molar ratios of Pt/Cu of the obtained bimetallic samples were determined by both inductively coupled plasma-atomic emission spectrometry (ICP-AES) analysis and energy dispersive X-ray spectrometry (EDS) as listed in Table 1, and the Pt/Cu ratios were in good agreement with the ratio of metal sources used in syntheses. A representative SEM image of the PtCu₂ nanocrystals was shown in Fig. 1a, which displayed uniform and well-dispersed nanoparticles, as also shown in the TEM image (Fig. 1b). The selected-area electron-diffraction (SAED) pattern (inset of

Fig. 1b) indicated that the PtCu₂ nanocrystals were crystalline. As shown in the magnified TEM images (Fig. 1c and d), the PtCu₂ nanocrystals exhibited concave surface with eight dendrites. The crystal lattice shown in Fig. 1e indicated that each nanocrystal particle was in good crystallinity. It has been reported that Pt nanoparticles with concave surface could enhance the electrocatalytic activity [30,31]. The high-angle annular dark-field scanning TEM (HAADF-STEM) image (Fig. 1f) also showed clearly the concave core with the surrounding dendrites. EELS elemental mapping are invaluable tools for understanding the metal distribution and overall composition of Pt-bimetallic nanoparticles [32–34], and here as shown in Fig. 1f, the high resolution elemental map of a concave dendritic PtCu₂ exhibited the feature of a core rich in Cu (red) and dendrites rich in Pt (green). The existence of the dendritic Pt nanoparticles implicated that they were formed via direct nucleation on the Cu core rather than random aggregation of Pt particles that might be formed through homogeneous nucleation in the solution (For interpretation of the references to color in this paragraph, the reader is referred to the web version of this article.).

Powder X-ray diffraction (XRD) patterns of the Pt–Cu nanocrystals were displayed in Fig. 2, and all the samples exhibited

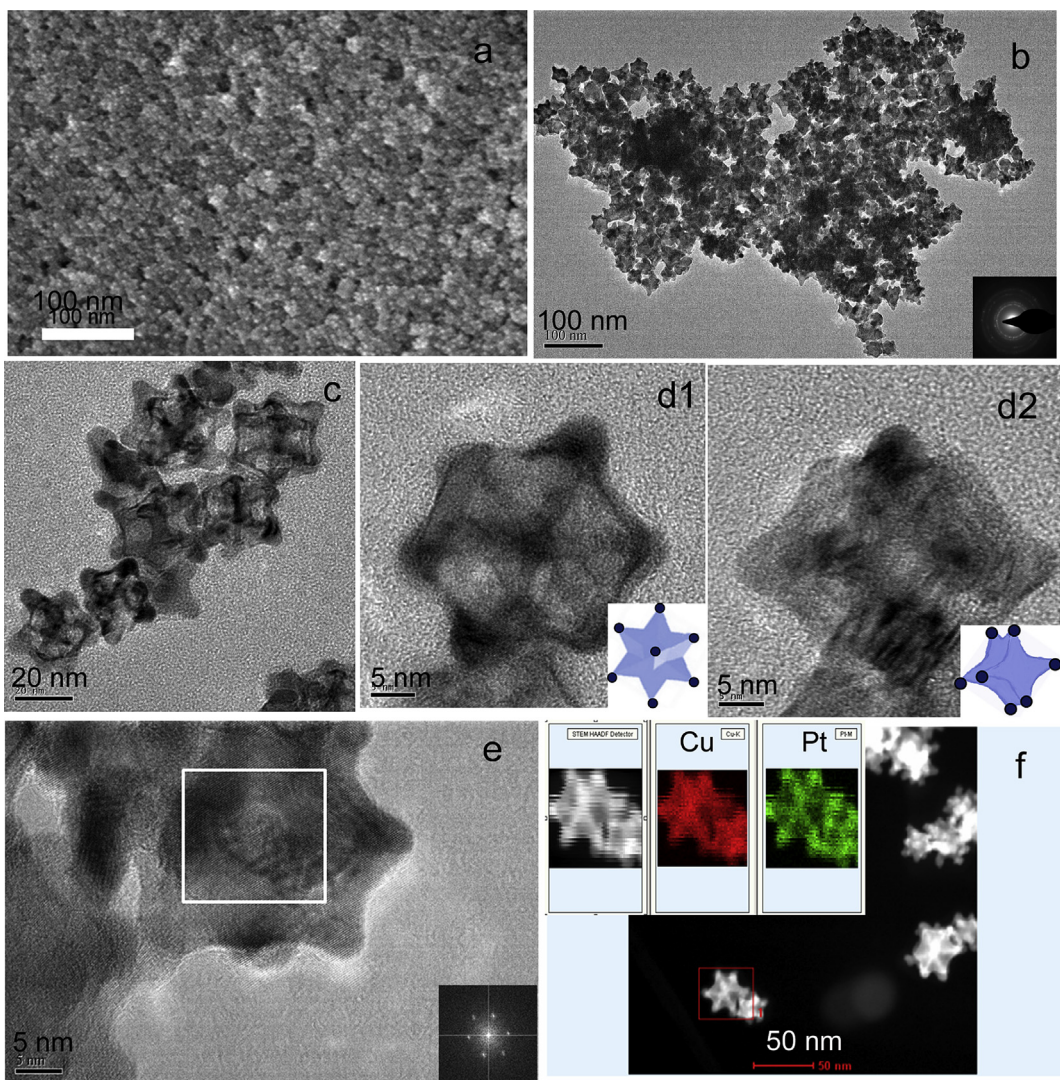


Fig. 1. a) FESEM image, b) TEM image inset: SAED pattern of PtCu₂ nanocrystals, c) magnified TEM image of concaved dendritic PtCu₂ nanocrystals, d1, d2) HRTEM images of PtCu₂, insets are the geometric models, e) HRTEM image of PtCu₂ nanocrystals, insets are the FFT (fast Fourier transition) patterns and f) HAADF-STEM image and corresponding elemental maps (Pt and Cu) of concave dendritic PtCu₂ nanocrystals.

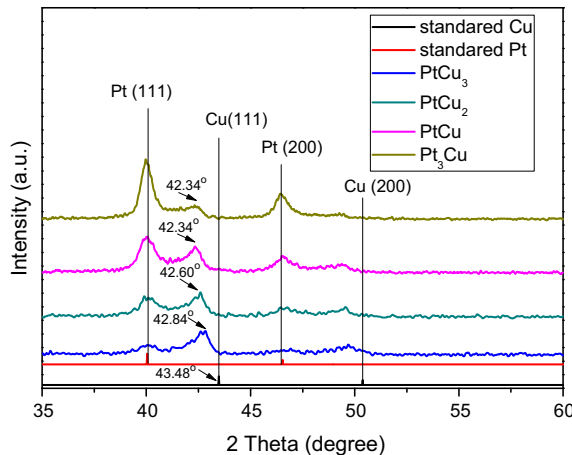


Fig. 2. XRD patterns of PtCu₃, PtCu₂, PtCu, Pt₃Cu, standard Pt and Cu.

similar disordered face-centered-cubic (fcc) structure. Compared with the standard (111) diffraction peaks, it was seen that for the Pt–Cu nanocrystals the Pt (111) diffraction peaks did not shift, implicating that most of the Pt was unalloyed, and this was in agreement with the element mapping of PtCu₂ particles (Fig. 1f). However, the Cu (111) diffraction peak of the Pt–Cu nanocrystals slightly shifted to 42.34°, 42.34°, 42.60° and 42.84° for Pt₃Cu, PtCu, PtCu₂ and PtCu₃ respectively, depending on the Pt proportion if compared with the standard diffraction peak of Cu (111) (43.48°). This indicated the formation of Cu–Pt alloy, however the proportion of Pt in the Cu–Pt alloy could be small because there was no indication of alloyed Pt peak in the XRD patterns.

TEM images of concave dendritic PtCu₃ and PtCu nanocrystals were shown as Fig. 3a and b, which displayed similar morphology of concave contour and dendrites. However, with the increase of the Pt portion in the bimetallic nanoparticles, the morphology of Pt₃Cu became nanosphere due to the formation of many small dendrites as shown in Fig. 4. The formation process of PtCu₂ concave dendritic nanocrystals was monitored by time-dependent experiments and the nanocrystals produced at different reaction durations were investigated by FESEM and TEM. The nanoparticles collected after reaction for 6 h displayed a uniform and concave morphology (Fig. 5a). With increasing of reaction time, the structure of concave dendritic nanocrystals continues to evolve and the concave dendritic structure can be clearly observed in the products obtained with reaction durations of 10 and 16 h (Fig. 5b and c). It has been

reported that poly(vinylpyrrolidone) (PVP) acted as a capping agent, reducing agent and stabilizer in the synthesis of metal nanocrystals [14]. Here the presence of PVP would probably slow down the reduction rates of Pt and Cu species; and a much slower reducing rate would give rise to the formation of concave nanocrystals, as revealed by Xia and co-workers in the synthesis of Pt concave nanocrystals [35]. Cu is relatively active, thus Cu nanocrystals are first formed although the standard reduction potential (E) for Cu²⁺/Cu (0.337 V vs SHE) is more negative than that of the [PtCl₆]²⁺/Pt pair (0.735 V vs SHE). The following galvanic replacement of Cu nanocrystals with Pt species in the solution finally led to the formation of PtCu₂ concave nanocrystals [36]. Based on these experiments, we suggest a mechanism in which galvanic replacement may play an important role in the synthesis of the concave and dendritic Pt–Cu bimetallic nanocrystals. As shown in Scheme 1, Pt–Cu nanocrystals were synthesized through co-reduction method in three major steps. Firstly Cu nanocubes were formed after reduction; the second step was selective nucleation of Pt at the edges and faces of the Cu-rich nanocubes via galvanic replacement to form nanoparticles with concave surface morphology; the third step was the growth of Pt-rich nanodendrites on the corners of the Cu-rich nanoparticles.

These concave dendritic Pt–Cu bimetallic nanocrystals with Pt rich dendrites would be of great interest as electrocatalysts. To perform the tests, Pt–Cu nanocrystals (NCs) were first deposited on a carbon black support (Vulcan XC-72) and the PtCu₂/C sample was also taken as an example to evaluate their potential as effective electrocatalysts. Its surface state was detected in 0.5 M H₂SO₄ solutions by cyclic voltammetry (CV). As shown in Fig. 6a, during the first potential cycling, a broad Cu dissolution feature was observed, with the peak at ~0.72 V (vs. RHE), which can be ascribed to the corrosion/dealloying of Cu from Pt–Cu nanocrystals as the dissolution of free, unalloyed Cu should occur at ~0.34 V [22]. In the subsequent cycles, the CV profiles quickly weakened, and behaved similar to a typical Pt-based electrode, with no apparent Cu-dissolution signals being observed. After a total of 150 cycles, the observed CV profiles became stable, indicating that Cu dissolution from the nanoparticles surface had either ceased or dropped to undetectable level. This dealloying process may induce surface re-arrangement, generating Pt-rich surfaces covering a core composed of Pt–Cu nanocrystals. Fig. 6b shows CV curves of Pt–Cu/C and commercial Pt/C (as shown in Fig. 7, Pt particle size \approx 3 nm) recorded at ambient temperature in N₂-purged 0.5 M H₂SO₄ solution at a sweep rate of 50 mV s⁻¹. The CV curves exhibited two distinct potentials regions associated with hydrogen adsorption/desorption processes between $-0.05 < E < +0.4$ V, and the formation of adsorbed hydroxyl species layer beyond ~0.5 V. The electrochemical active surface area (ECSA) was calculated by

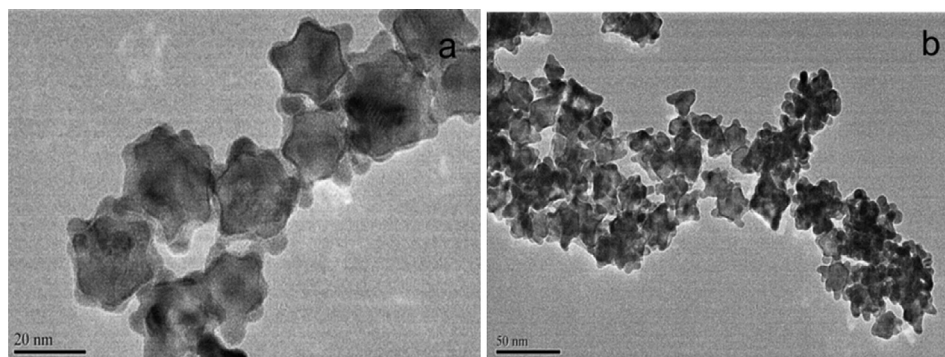


Fig. 3. TEM of concave dendritic PtCu₃ and PtCu.

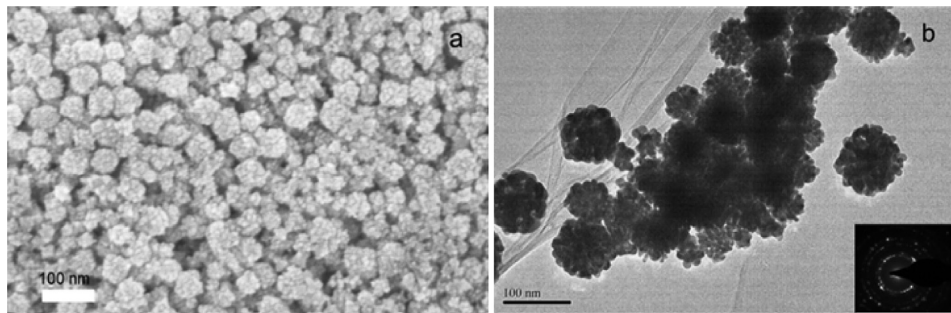


Fig. 4. a, b) FESEM and TEM of nanosphere Pt_3Cu nanocrystals. Inset of b) SAED pattern of Pt_3Cu nanosphere.

integrating the charge passing the electrode during the hydrogen adsorption/desorption region after the correction for the double layer formation and assuming a value of $210 \mu\text{C cm}^{-2}$ for the adsorption of a hydrogen monolayer. The ECSAs (the ECSA per unit

weight of Pt) estimated from the hydrogen adsorption peaks were $60.3 \text{ m}^2 \text{ g}^{-1}$ for $\text{Pt}_3\text{Cu}/\text{C}$ nanospheres, $70.2 \text{ m}^2 \text{ g}^{-1}$ for PtCu/C nanocrystals, $64.2 \text{ m}^2 \text{ g}^{-1}$ for PtCu_2/C , and $53.1 \text{ m}^2 \text{ g}^{-1}$ for PtCu_3/C nanocrystals, respectively, which were lower than that of the Pt/C catalyst ($82.1 \text{ m}^2 \text{ g}^{-1}$) (Fig. 6c). The loss of ECSA with cycling was plotted in Fig. 6d. After 3000 cycles, the PtCu_2/C catalyst lost only 24% of the initial Pt ECSA, while the commercial Pt/C catalysts lost 50% of their initial ECSA. The results demonstrated that concave and dendritic PtCu_2/C nanocrystals have significantly higher stability than that of the commercial Pt/C catalyst.

Next, we investigated the catalytic activity of the $\text{Pt}-\text{Cu}/\text{C}$ nanocrystals toward methanol oxidation. In order to compare the mass activity of different catalysts, the kinetic current was calculated from the MOR curve by using mass-transport correction and normalized to the loading amount of Pt. Fig. 8a displays the CV (after 10 cycles of CV sweeps from 0.1 to 1.0 V (vs. RHE) at the scan rate of 20 mV s^{-1}) profiles in $0.5 \text{ M H}_2\text{SO}_4$ and $1.0 \text{ M CH}_3\text{OH}$ mixed solution, and the mass activity (normalized in references to the loading amount of Pt) of the PtCu_2/C sample was 3.3 times higher than that of Pt/C . In methanol oxidation, the first anodic peak is usually ascribed to the oxidation of methanol molecules on the electrode surface, while the backward anodic peak is generally attributed to the continuous oxidation of incompletely oxidized carbonaceous intermediates accumulated on the catalyst surface during the forward scan, such as CO , HCOO^- , and HCO^- [37]. Consequently, the ratio of current densities for these two anodic peaks, I_f/I_b , was generally used to evaluate the poison tolerance of Pt catalysts [4]. The observation of much higher I_f/I_b values for PtCu_2/C (2.28 vs. 0.94 on Pt/C) implicated that methanol molecules can be more effectively oxidized on PtCu_2 during the forward potential scan, generating relatively less poisoning species as compared to Pt/C . As summarized in Table 2, the peak current densities of methanol oxidation in the forward (positive) potential (J_f) were: $\text{PtCu}_2/\text{C} > \text{PtCu}/\text{C} > \text{PtCu}_3/\text{C} > \text{Pt}/\text{C} > \text{Pt}_3\text{Cu}/\text{C}$. To further explore the observed enhancement of the electrocatalytic activity and CO-tolerance, we carried out a chronoamperometry (CA) experiment. From Fig. 8b, CA curves (performed at 0.7 V for 5 h)

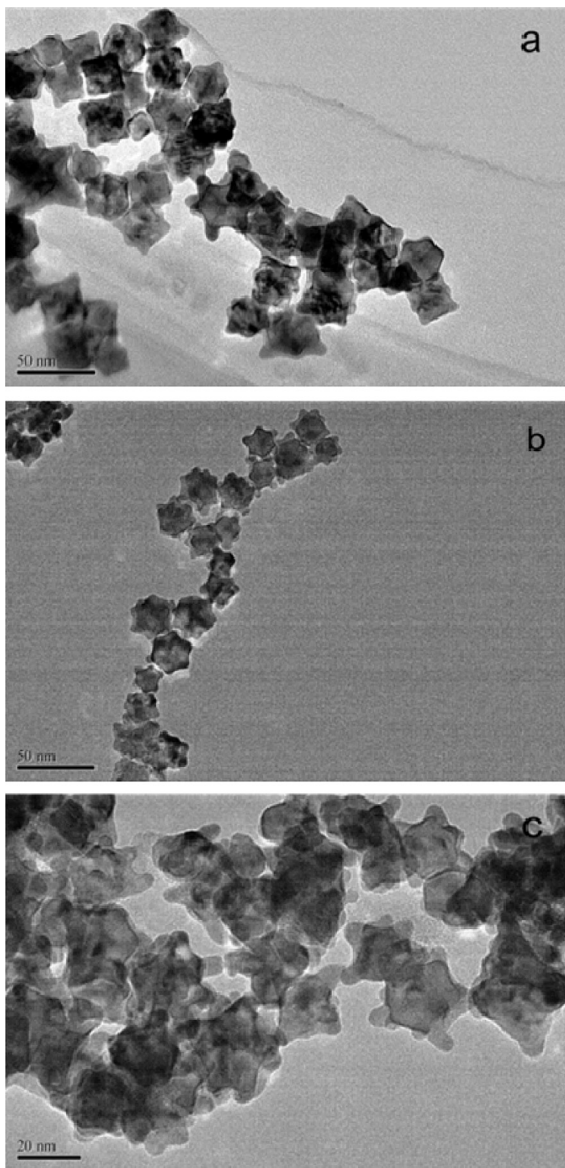


Fig. 5. TEM image of products obtained with different reaction durations: a) 6 h; b) 10 h; c) 16 h.



Scheme 1. The two major steps in the progressive formation of $\text{Pt}-\text{Cu}$ concave and dendritic nanocrystals. Step 1: selective nucleation of Pt at the edges and faces of the Cu-rich nanocubes owing to the capping of side faces by PVP. Step 2: the growth of Pt-rich nanodentrites on the corners of the Cu-rich nanocubes.

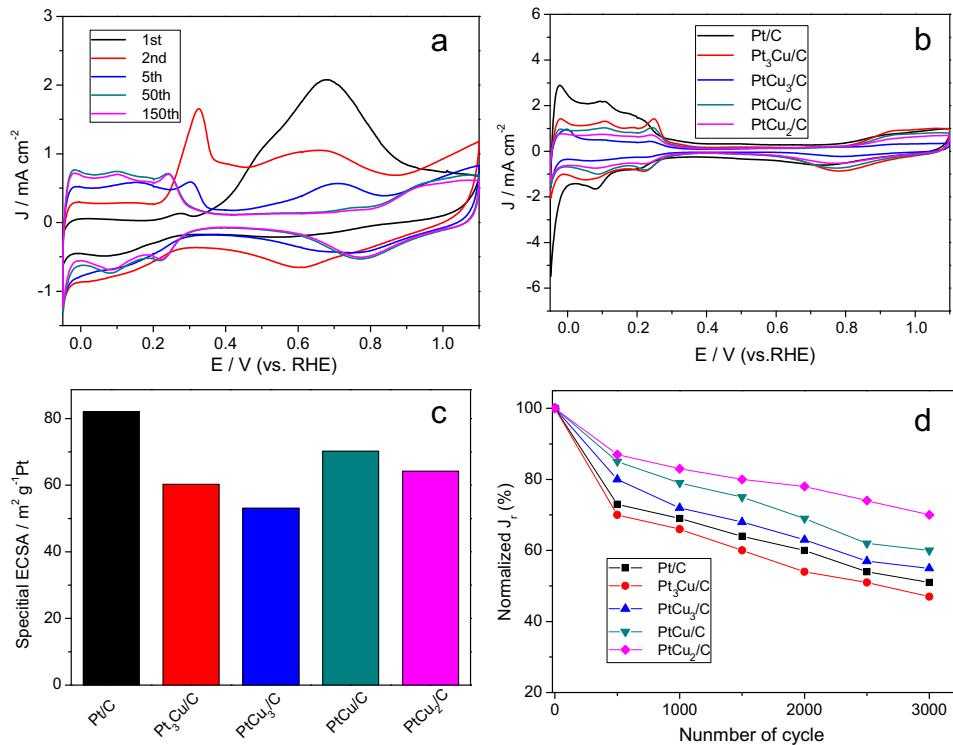


Fig. 6. a) Cyclic voltammetric (CV) profiles of PtCu₂ nanocrystals at 50 mV s⁻¹. b) CV profiles of Pt–Cu/C (PtCu₃, PtCu₂, PtCu and Pt₃Cu) and commercial Pt/C catalysts in a 0.5 M H₂SO₄ solution. c) Specific ECSAs for the Pt–Cu/C and commercial Pt/C catalysts. d) Loss of ECSA of Pt–Cu/C and commercial Pt/C catalysts as a function of cycling number.

indicated that the current density of concave dendritic PtCu₂/C nanocrystal was higher than that of other concave dendritic PtCu/C, PtCu₃/C, nanosphere Pt₃Cu/C and the commercial Pt/C electrocatalyst for the entire time course, which further verified that the concave dendritic PtCu₂/C bimetallic nanocrystals exhibited better electrocatalytic performance in the methanol oxidation reaction. The specific activity kinetic current was calculated from the ECSA and mass activity. At ambient temperature, the PtCu₂/C nanocrystals exhibited a specific activity of 9.4 mA m⁻² on the basis of Pt at 0.7 V versus RHE, which was 4.1

times greater than that of Pt/C (2.3 mA m⁻²). The specific activity of Pt₃Cu/C, PtCu₃/C, and PtCu/C catalysts were 1.3, 5.0, and 6.2 mA m⁻² (Table 3), respectively.

CO stripping experiments were also carried out and the results are shown in Fig. 9. Prior to CO adsorption, the electrolytes were deoxygenated by bubbling with N₂ for 30 min. For CO stripping experiments, CO was adsorbed on the pre-cleaned electrode by holding the potential at 0.1 V (vs. RHE) for 5 min by bubbling CO gas through the electrolyte solution. CO dissolved in the electrolyte solution was then removed by purging nitrogen through the

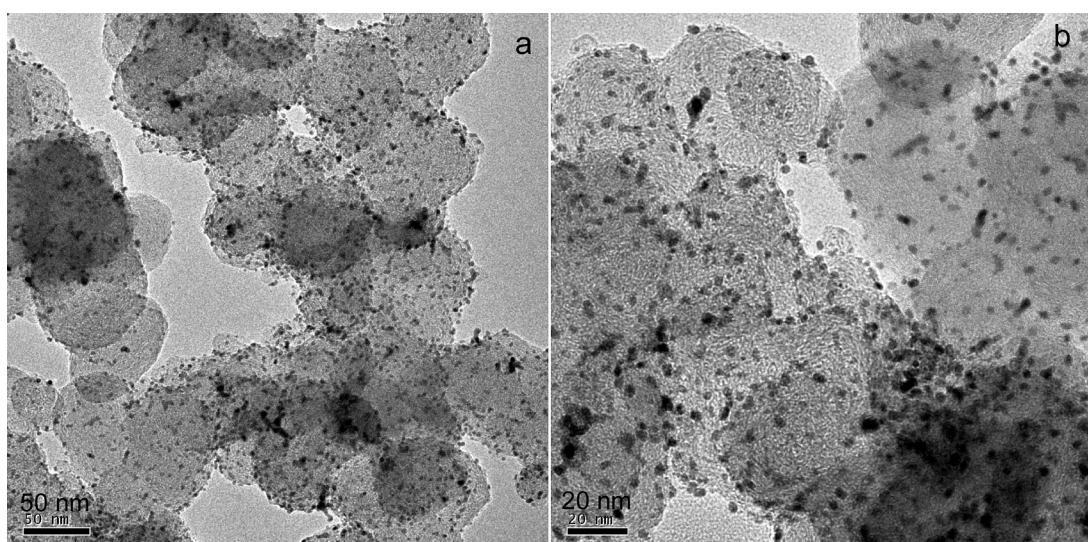


Fig. 7. a, b) TEM and magnified TEM of Commercial Pt (JM, 20%) electrocatalyst.

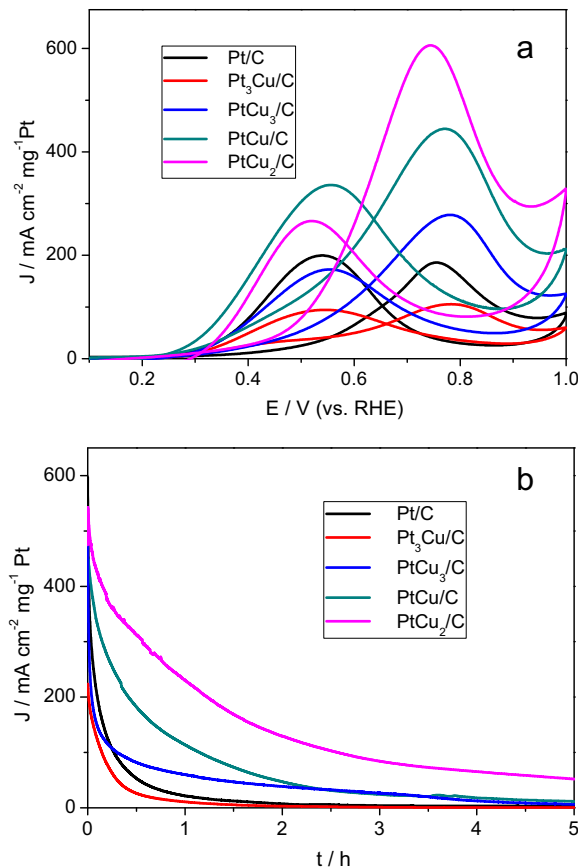


Fig. 8. a, b) CV and chronoamperometric (CA) results of CH_3OH oxidation on Pt–Cu/C and commercial Pt/C catalysts in a 0.5 M H_2SO_4 + 1 M CH_3OH solution (20 mV s^{-1}). CA curves were recorded at 0.7 V (vs. RHE). The data is given as kinetic current densities (J_k) normalized in references to the loading amount of Pt.

Table 2

Forward peak potential (E_f), forward peak current density (J_f), reverse peak potential (E_b), reverse peak current density (J_b), and J_f/J_b for methanol oxidation on different Pt-based catalysts recorded in 0.1 M H_2SO_4 + 1 M CH_3OH .

Entry	Catalysts	E_f/V	$J_f/\text{mA mg}^{-1}$	E_b/V	$J_b/\text{mA mg}^{-1}$	J_f/J_b
1	PtCu_3/C	0.78	278.2	0.55	172.7	1.61
2	PtCu_2/C	0.74	606.0	0.52	265.7	2.28
3	PtCu/C	0.78	439.2	0.55	336.1	1.31
4	$\text{Pt}_3\text{Cu}/\text{C}$	0.78	105.6	0.56	94.5	1.12
5	Pt/C	0.75	185.5	0.54	199.7	0.93

Table 3

Catalyst composition, electrochemical surface area, and activities of Pt–Cu/C and Pt/C MOR catalysts (at 0.70 V).

Catalyst	$\text{ECSA}/\text{m}^2 \text{g}^{-1}$	Mass activity/ mA mg^{-1}	Specific activity/ mA m^{-2}
PtCu_3/C	53.1	267.4	5.0
PtCu_2/C	64.2	604.8	9.4
PtCu/C	70.2	437.4	6.2
$\text{Pt}_3\text{Cu}/\text{C}$	60.3	101.4	1.3
Pt/C	82.1	185.5	2.3

solution for 15 min. For Pt/C catalyst, a sharp peak was observed at around 0.80 V. Compared to Pt/C catalyst, CO stripping voltammogram of PtCu_3/C , PtCu_2/C , PtCu/C and $\text{Pt}_3\text{Cu}/\text{C}$ catalysts presented a sharp peak at a potential of 0.74, 0.75, 0.77 and 0.81 V, suggesting a higher CO oxidation activity on PtCu_3/C , PtCu_2/C and PtCu/C catalysts because of the slightly more negative potential.

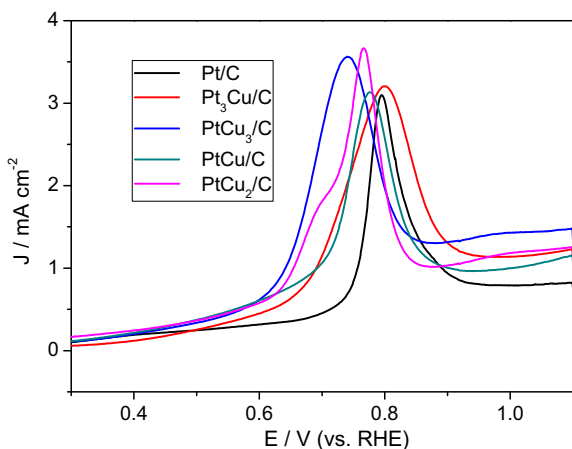


Fig. 9. CO stripping curves of the Pt–Cu/C and Pt/C catalysts in 0.5 M H_2SO_4 .

What's more, the onset potential of PtCu_3/C , PtCu_2/C and PtCu/C catalysts was lower than that of Pt/C, which indicated higher CO tolerance.

4. Conclusions

In summary, this work presented a simple one-pot synthesis of concave dendritic PtCu_x ($x = 1, 2$ and 3) nanocrystals and Pt_3Cu nanosphere through a galvanic replacement mechanism between preformed Cu nanocrystals and Pt species and a comparative investigation of the electrocatalytic activity and stability in the methanol oxidation process. The as-prepared concave dendritic PtCu_2/C nanocrystals exhibit enhanced electrocatalytic activity in the methanol oxidation reaction compared with other concave PtCu/C , PtCu_3/C , $\text{Pt}_3\text{Cu}/\text{C}$, and commercial Pt/C electrocatalyst. Such superior overall electrocatalytic performance, and especially the higher CO tolerance, suggests that the PtCu_2/C catalyst could be regarded as a promising anode catalyst in the fuel cell. This enhanced performance toward the methanol oxidation could be attributed to the concave structure and possible synergistic effect of Pt and Cu components.

Acknowledgements

This work was supported by NSFC (20873070, 20973095), Tianjin Natural Science Research Fund (13JCYBJC18300), National Basic Research Program of China (2009CB623502), RFDP (20120031110005) and NCET of Ministry of Education (NCET-07-0448).

References

- Y.H. Bing, H.S. Liu, L. Zhang, D. Ghosh, J.J. Zhang, Chem. Soc. Rev. 39 (2010) 2184–2202.
- P. Strasser, Rev. Chem. Eng. 25 (2009) 255–295.
- C.Y. Wang, Chem. Rev. 104 (2004) 4727–4765.
- S. Wasmus, A. Kuver, J. Electroanal. Chem. 461 (1999) 14–31.
- M.K. Jeon, J.S. Cooper, P.J. McGinn, J. Power Sources 185 (2008) 913–916.
- H.S. Liu, C.J. Song, L. Zhang, J.J. Zhang, H.J. Wang, D.P. Wilkinson, J. Power Sources 155 (2006) 95–110.
- A.S. Arico, S. Srinivasan, V. Antonucci, Fuel Cells 1 (2001) 133–161.
- S.J. Guo, S. Zhang, X.L. Sun, S.H. Sun, J. Am. Chem. Soc. 133 (2011) 15354–15357.
- S.J. Guo, S.J. Dong, E.K. Wang, ACS Nano 4 (2010) 547–555.
- J.Y. Chen, B. Lim, E.P. Lee, Y.N. Xia, Nano Today 4 (2009) 81–95.
- H.X. Wu, H.J. Li, Y.J. Zhai, X.L. Xu, Y.D. Jin, Adv. Mater. 24 (2012) 1594–1597.
- A.C. Chen, P. Holt-Hindle, Chem. Rev. 110 (2010) 3767–3804.
- S.J. Yoo, T.Y. Jeon, K.S. Kim, T.H. Lim, Y.E. Sung, Phys. Chem. Chem. Phys. 12 (2010) 15240–15246.
- A.X. Yin, X.Q. Min, W. Zhu, W.C. Liu, Y.W. Zhang, C.H. Yan, Chem.—Eur. J. 18 (2012) 777–782.

- [15] J. Kugai, T. Moriya, S. Seino, T. Nakagawa, Y. Ohkubo, H. Nitani, H. Daimon, T.A. Yamamoto, *Int. J. Hydrogen Energy* 37 (2012) 4787–4797.
- [16] X.Q. Huang, Z.P. Zhao, J.M. Fan, Y.M. Tan, N.F. Zheng, *J. Am. Chem. Soc.* 133 (2011) 4718–4721.
- [17] Z.Q. Niu, D.S. Wang, R. Yu, Q. Peng, Y.D. Li, *Chem. Sci.* 3 (2012) 1925–1929.
- [18] Y. Liu, D.G. Li, V.R. Stamenkovic, S. Soled, J.D. Henao, S.H. Sun, *ACS Catal.* 1 (2011) 1719–1723.
- [19] H.Z. Yang, J. Zhang, K. Sun, S.Z. Zou, J.Y. Fang, *Angew. Chem., Int. Ed.* 49 (2010) 6848–6851.
- [20] S. Papadimitriou, S. Aramyanov, E. Valova, A. Hubin, O. Steenhaut, E. Pavlidou, G. Kokkinidis, S. Sotiropoulos, *J. Phys. Chem. C* 114 (2010) 5217–5223.
- [21] D. Xu, Z.P. Liu, H.Z. Yang, Q.S. Liu, J. Zhang, J.Y. Fang, S.Z. Zou, K. Sun, *Angew. Chem., Int. Ed.* 48 (2009) 4217–4221.
- [22] S. Koh, P. Strasser, *J. Am. Chem. Soc.* 129 (2007) 12624–12625.
- [23] B.Y. Xia, H.B. Wu, X. Wang, X.W. Lou, *J. Am. Chem. Soc.* 134 (2012) 13934–13937.
- [24] J. Sa, N. Barrabes, E. Kleymenov, C. Lin, K. Fottinger, O.V. Safonova, J. Szlachetko, J.A. van Bokhoven, M. Nachtegaal, A. Urakawa, G.A. Crespo, G. Rupprechter, *Catal. Sci. Technol.* 2 (2012) 794–799.
- [25] B.I. Podlovchenko, T.D. Gladysheva, V.A. Krivchenko, Y.M. Maksimov, A.Y. Filatov, L.V. Yashina, *Mendeleev Commun.* 22 (2012) 203–205.
- [26] D.L. Wang, Y.C. Yu, H.L.L. Xin, R. Hovden, P. Ercius, J.A. Mundy, H. Chen, J.H. Richard, D.A. Muller, F.J. DiSalvo, H.D. Abruna, *Nano Lett.* 12 (2012) 5230–5238.
- [27] P. Strasser, S. Koh, T. Anniyev, J. Greeley, K. More, C.F. Yu, Z.C. Liu, S. Kaya, D. Nordlund, H. Ogasawara, M.F. Toney, A. Nilsson, *Nat. Chem.* 2 (2010) 454–460.
- [28] P. Mani, R. Srivastava, P. Strasser, *J. Phys. Chem. C* 112 (2008) 2770–2778.
- [29] R. Yang, J. Leisch, P. Strasser, M.F. Toney, *Chem. Mater.* 22 (2010) 4712–4720.
- [30] M.S. Jin, H. Zhang, Z.X. Xie, Y.N. Xia, *Angew. Chem., Int. Ed.* 50 (2011) 7850–7854.
- [31] Y. Wu, D. Wang, Z. Niu, P. Chen, G. Zhou, Y. Li, *Angew. Chem., Int. Ed.* 124 (2012) 12692–12696.
- [32] D.L. Wang, H.L. Xin, Y.C. Yu, H.S. Wang, E. Rus, D.A. Muller, H.D. Abruna, *J. Am. Chem. Soc.* 132 (2010) 17664–17666.
- [33] S.F. Xie, N. Lu, Z.X. Xie, J.G. Wang, M.J. Kim, Y.N. Xia, *Angew. Chem., Int. Ed.* 51 (2012) 10266–10270.
- [34] V. Mazumder, M.F. Chi, M.N. Mankin, Y. Liu, O. Metin, D.H. Sun, K.L. More, S.H. Sun, *Nano Lett.* 12 (2012) 1102–1106.
- [35] T. Yu, D.Y. Kim, H. Zhang, Y.N. Xia, *Angew. Chem., Int. Ed.* 50 (2011) 2773–2777.
- [36] D.S. Wang, Y.D. Li, *Adv. Mater.* 23 (2011) 1044–1060.
- [37] Y.X. Chen, A. Miki, S. Ye, H. Sakai, M. Osawa, *J. Am. Chem. Soc.* 125 (2003) 3680–3681.